

www.acsnano.org

Amyloid Fibrillation of a Ninjurin-1-Derived α -Helical Peptide: Structural Insights into **Conformational Transition**

Meijiao Wang, Wencheng Xia, Dan Zhao, Zhaoyi Zhai, Rongjing Chen, Xue Bai, Zhe Zhang, Hao Fan, Jian-Ping Zhang,* Cong Liu,* and Fang Jiao*



See https://pubs.acs.org/sharingguidelines for options on how to legitimately share published articles

Downloaded via INST OF PHYSICS on October 22, 2025 at 03:38:47 (UTC).

Cite This: ACS Nano 2025, 19, 35977-35991



ACCESS I III Metrics & More Article Recommendations Supporting Information

ABSTRACT: Amyloid fibrils, defined by their cross-\(\beta \) architecture, are central to both disease and function, yet the molecular principles governing their formation remain incompletely understood. Ninjurin-1 (NINJ1), a membrane protein essential for plasma membrane rupture (PMR) during cell death, contains an N-terminal amphipathic α helix. Here, we investigate a key peptide fragment of this region (residues 40-69, HE30) and uncover its membranedisruptive activity, self-assembly, and structural transitions. Monomeric HE30 reorganizes lipids to induce membrane thinning while undergoing an environmentally responsive α -helix-to- β -sheet transition that drives amyloid fibril formation. Fibrils formed at physiological temperatures are predominantly nontwisted, but elevated temperatures induce left-handed twisted structures with variable pitches and lengths, and even result in high-order superhelical bundles. We further resolved the twisted fibril structures of HE30 by cryo-EM, revealing two distinct fibril polymorphs stabilized by both hydrophobic and electrostatic interactions. Consistently, salts inhibit HE30 fibrillation, emphasizing the role of electrostatic interactions in stabilizing fibrils. Moreover, acidic conditions (~pH 4.4) promote fibril formation, whereas alkaline conditions lead to disassembly into α -helical monomers in a reversible manner. In situ AFM tracking reveals the asymmetric growth of fibrils, where one end elongates faster and the opposite end exhibits slower growth or complete inhibition. Functionally, HE30 fibrils are nontoxic and act as scaffolds for the temperature-controlled assembly of gold nanoparticle (AuNPs) superstructures. These findings not only advance our understanding of NINI1-induced PMR but also provide a detailed structural basis for HE30 fibril formation via α -helix to β -sheet transitions and underscore their potential as building blocks for fibril-based biomaterials.

KEYWORDS: NINJ1, amyloid fibril, hierarchical self-assembly, gold nanoparticle superstructures, AFM

Amyloid fibrils are a prominent supramolecular architecture adopted by diverse proteins and peptides, facilitating a wide range of biological functions in both physiological and pathological contexts.¹⁻⁴ Broadly, amyloids are classified into two categories: pathological and functional amyloids. Pathological amyloids refer to fibrillar aggregates implicated in neurodegenerative disorders, including Alzheimer's disease

Received: August 28, 2025 September 24, 2025 Revised: Accepted: September 24, 2025 Published: October 2, 2025





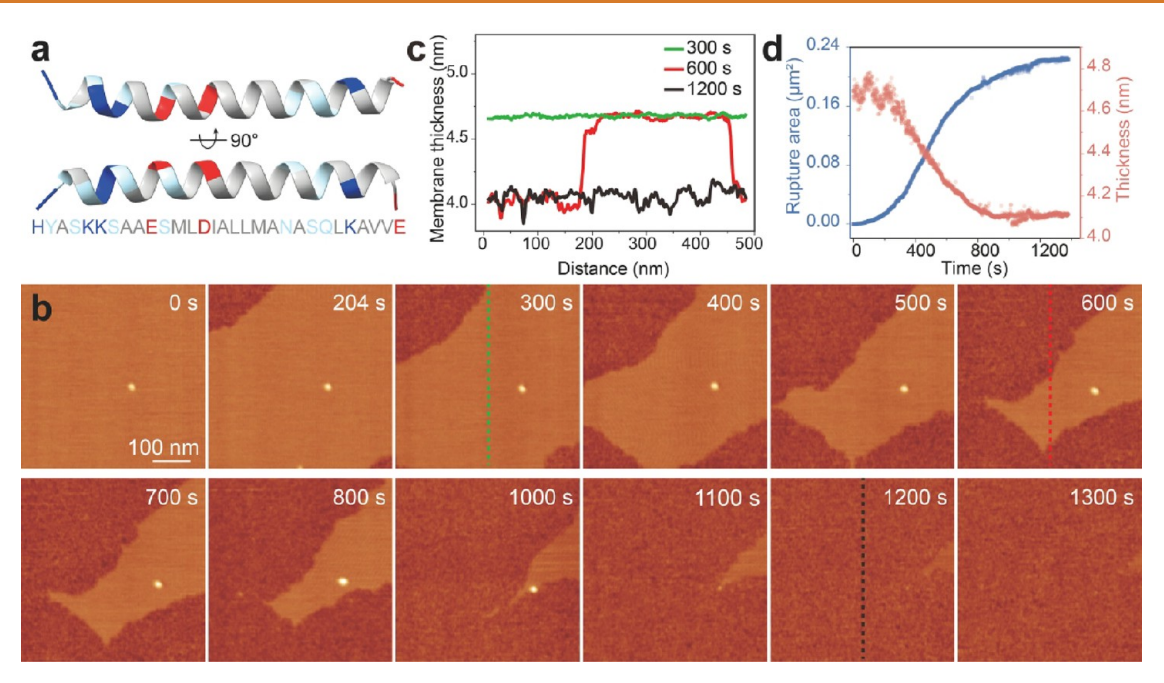


Figure 1. Membrane disruption induced by HE30. (a) HE30 structure predicted by AlphaFold3 with its sequence annotated: blue indicates positively charged residues, gray represents hydrophobic residues, light blue donates polar residues, and red marks negatively charged residues. (b) HS-AFM frames showing membrane disruption upon incubation of 313 μ M HE30 monomer on a SLB composed of DOPC:DOPS:DOPE = 8:1:1. (c) Height profiles along the dashed lines at 300, 600, and 1200 s in (b). (d) Quantitative analysis of the membrane rupture area and reduction in membrane thickness over time from the data in (b).

(AD), Parkinson's disease (PD), and Type-2 diabetes (T2D), where aberrant protein misfolding and aggregation drive disease pathology. ⁶⁻⁹ In contrast, functional amyloids serve conserved biological roles across all three life kingdoms—appearing in bacteria, fungi, protozoa, plants, insects, marine organisms, and mammals, including humans—where they contribute to processes ranging from biofilm formation to structural scaffolding. ¹⁰⁻¹⁸

Structurally, amyloid fibrils consist of a rigid core region surrounded by flexible flanking regions. During fibrillation, specific segments of the protein, known as the fibril core, undergo conformational rearrangement to adopt a cross- β spine structure. This core formation is marked by β -sheet stacking—a characteristic of the cross- β architecture—stabilized through extensive hydrogen bonding. ¹⁹ Fibril formation often involves secondary structure transitions such as the conversion of random coils or α -helices into β -sheets, culminating in the deposition of stable, yet insoluble, fibrillar assemblies. Despite significant progress, the molecular mechanisms governing amyloid fibril formation and the factors regulating their structural polymorphism are poorly understood. Addressing these gaps is critical for elucidating the stability and pathogenicity of amyloids and unlocking their potential as functional biomaterials in biomedical and biotechnological applications.

NINJ1 is a 16-KDa membrane protein that is widely expressed in all higher eukaryotes. NINJ1 was initially identified for its role in cell adhesion $^{20-22}$ and recently established as a key mediator in plasma membrane rupture (PMR) in many cell-death pathways, such as pyroptosis, toxin- or $\rm H_2O_2$ -induced necrosis, and postapoptosis lysis. $^{23-27}$ In its inactive state, NINJ1 adopts a three α -helix structure, which includes two transmembrane α -helices and an N-terminal domain (residues 1–78) containing an amphipathic α -helix (residues 37–71). 28 Early studies suggested that the N-terminal α -helix of inactive NINJ1 was

positioned extracellularly;^{21,23} however, recent cryo-EM data indicate it may instead stay as a continuous transmembrane helix.²⁸

Upon activation, the N-terminal α -helix undergoes conformational rearrangement, forming a kink at residue around 55 that divides it into two helical segments.²⁹⁻³¹ This structural reorganization facilitates NINJ1 oligomerization and triggers PMR. Recent cryo-EM studies have yielded two conflicting models for NINJ1-mediated PMR: one suggests that NINJ1 assembles into amphipathic filaments or pores with a hydrophilic conduit,²⁹ while the other proposes the formation of nanodiscs with a hydrophilic exterior, acting as "cookie cutters" to perforate the membrane. 30,31 Despite their differences, both models emphasize the pivotal role of the N-terminal α -helix in driving the NINJ1 assembly and membrane rupture. Synthetic peptides corresponding to residues 40-69 (termed HE30) within this region demonstrate membrane-disruptive potential, evidenced by their ability to disrupt synthetic liposome membranes.²³ Elucidating the membrane interactions and selfassembly of HE30 can thus provide mechanistic insights into NINJ1-mediated PMR and contribute to the development of novel peptide biomaterials.

In this study, we systematically investigate the membrane interactions, assembly, and structural transitions of HE30 under various conditions, using advanced techniques including AlphaFold, atomic force microscopy (AFM), transmission electron microscopy (TEM), circular dichroism (CD), and cryo-electron microscopy (cryo-EM). Our findings demonstrate that monomeric HE30 induces membrane thinning and undergoes a transition from an α -helical conformation to β -sheet to form amyloid fibrils, with fibril morphology and growth highly dependent on environmental factors, including temperature, pH, and ionic strength. HE30 fibrils neither induce membrane rupture nor exhibit cytotoxicity but instead can be

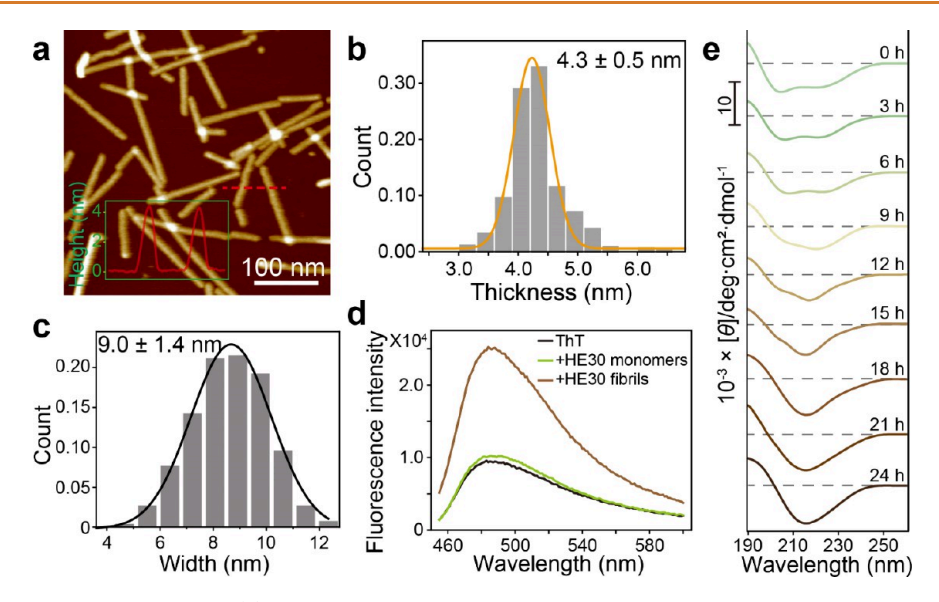


Figure 2. Formation of HE30 amyloid fibrils. (a) AFM image of 100 μ M HE30 after incubation at 37 °C for 24 h. The inset shows the height profile along the red dashed line. (b) Thickness distribution of HE30 fibrils with an orange line showing Gaussian fit (total count: 469), mean \pm S.D.: 4.3 \pm 0.5 nm. (c) Width distribution of HE30 fibrils with a blue line showing Gaussian fit (total count: 260), mean \pm S.D.: 9.0 \pm 1.4 nm. (d) ThT fluorescence spectra of 200 μ M ThT alone and coincubation of HE30 monomers or preformed fibrils (100 μ M HE30 incubated in water containing 0.8% ACN at 37 °C for 24 h) with ThT. (e) CD spectra of 100 μ M HE30 incubated at 37 °C over time intervals of 0, 3, 6, 9, 12, 15, and 24 h, showing the transition from α-helix to β-sheet configuration during fibril formation, scale bar: $10^{-2} \times [\theta]/\text{deg·cm}^2 \cdot \text{dmol}^{-1}$.

harnessed as temperature-responsive scaffolds to organize gold nanoparticles into straight and twisted superstructures.

RESULTS

Membrane Disruption Induced by HE30 Monomers. The HE30 peptide (sequence HYASKKSAAESMLDIALLMA-NASQLKAVVE), characterized by amphipathic properties (Figure 1a), was synthesized with high purity (98.69%), as confirmed by HPLC and mass spectrometry (Figures S1 and S2). AlphaFold3 predictions consistently indicated an α-helical fold across all five top models (Figure S3a), in agreement with cryo-EM data of the inactive NINJ1 structure that revealed a corresponding α-helix (Figure S3b). The close alignment between predicted HE30 structures and the cryo-EM model suggests that HE30 likely maintains its α-helical conformation in physiological solutions (Figure S3c).

Due to its amphiphilic nature, HE30 was difficult to fully dissolve in pure water; therefore, 0.8% acetonitrile (ACN) was added to achieve complete solubilization for all experiments. Size-exclusion chromatography (SEC) and AFM imaging demonstrated that at 100 μ M, HE30 exists predominantly in a monomeric state, showing small clusters that are only a few nanometers in size (Figure S4). Circular dichroism (CD) spectra confirmed its α -helical structure (Figure 2e), which was further verified by a D-amino-acid analog of HE30 (Figure S5).

Previous studies reported that HE30 exhibits membrane-disruptive activity as measured by cargo-release assays. ²³ To probe its interaction with membranes, we applied HE30 monomers to supported lipid bilayers (SLB, DOPC:DOPS:-DOPE 8:1:1) and monitored the process by *in situ* high-speed AFM (HS-AFM). Interestingly, at 313 μ M, HE30 induced bilayer thinning of only a few angstroms without detectable pore formation (Figure 1b-d, Movie S1). This suggests that HE30 adsorbs onto the bilayer surface, inserts in parallel or oblique orientations, and partitions into the membrane to reorganize lipids, thereby enhancing permeability without creating stable pores (Figure 9). This behavior resembles the interfacial-

activity, or "carpet-like" mechanism reported for many α -helical antimicrobial peptides, ^{32,33} which disrupt membranes by thinning and defect formation rather than by assembling stable transmembrane pores. Together, our data support a nonlytic, interfacial mechanism for HE30, distinguishing it from strongly pore-forming helices and positioning it among amphipathic peptides whose activity arises from lipid reorganization and defect-mediated leakage.

HE30 Self-Assembles into Amyloid Fibril. The NINJ1derived peptide HE30 displayed atypical membrane activity compared with that of canonical α -helical antimicrobial peptides (AMPs). Typical AMPs disrupt membranes at submicromolar concentrations (peptide-to-lipid ratio far below 1:1), 33,34 HE30 required a much higher concentration (313 μ M) to induce bilayer disruption, as observed by HS-AFM (Figure 1a, Movie S1) and no disruption was detected at submicromolar levels (data not shown). Consistently, giant unilamellar vesicles (GUVs) leakage assays revealed negligible dye release even at a peptide-to-lipid ratio of 3:1 (Figure S6), and HE30 exhibited no cytotoxicity toward human lung epithelial, embryonic kidney (HEK293T), or lung cancer cells, in some cases even promoting proliferation (Figures S7 and S8a). These results, together with prior liposomal cargo-release experiments performed at an extremely high peptide-to-lipid ratio (~157:1),²³ suggest that HE30 possesses only weak membrane-disruptive capacity, likely due to instability of its α -helical state in aqueous solution.

Intriguingly, upon incubation at 37 °C for 24 h, HE30 assembled into fibrils (Figure 2a). These fibrils measure 4.3 ± 0.5 nm in thickness and 9.0 ± 1.4 nm in width (Figure 2b,c) and display characteristic β -sheet structures (Figure 2e). Timelapsed CD spectra and enhanced fluorescence emission in Thioflavin T (ThT) assays confirmed the structural transition of HE30 from an α -helix to a β -sheet upon fibril formation (Figure 2d,e), underscoring its amyloidogenic potential. TEM further demonstrated the existence of fibrils after 24 h of coincubation with ThT (Figure S9). Once formed, the HE30 fibrils exhibit

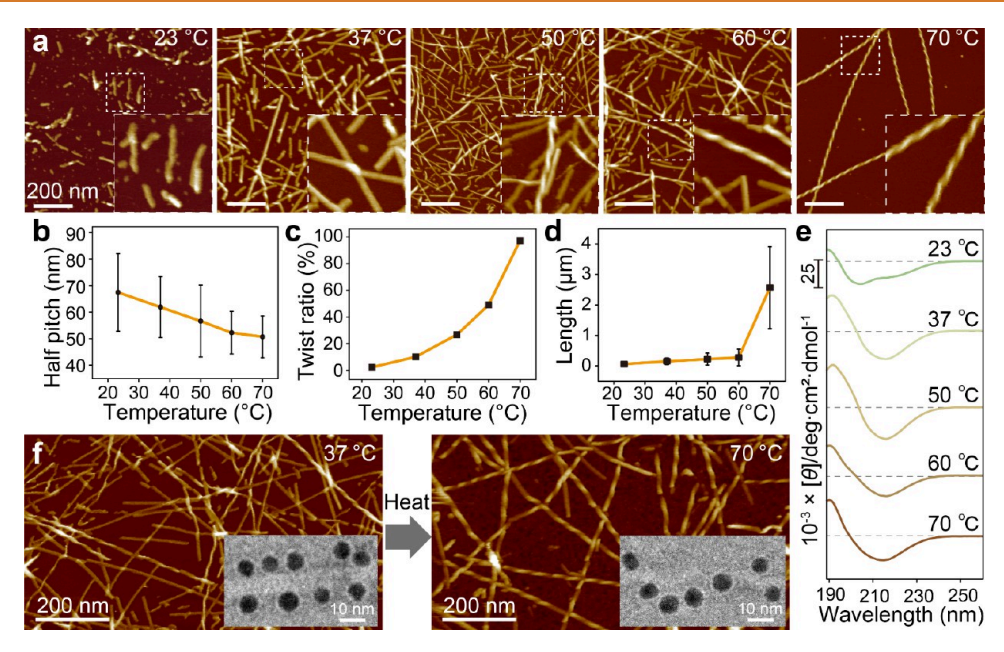


Figure 3. Temperature-dependent fibril formation of HE30. (a) AFM topographies of 100 μ M HE30 after 24 h incubation at various temperature: 23, 37, 50, 60, and 70 °C. The inset shows an enlarged view of the area within the white dashed box, scale bar: 200 nm. (b) Effect of temperature on the half-twisted pitch of HE30 fibrils. (c) Effect of temperature on the ratio of HE30 twisted fibrils. (d) Effect of temperature on the length of HE30 fibrils. (e) CD spectra of HE30 after 24 h incubation at various temperature: 23, 37, 50, 60, and 70 °C, scale bar: 25 × 10⁻³ × $[\theta]/\text{deg·cm}^2\text{-dmol}^{-1}$. (f) Twisted transition observed following a 24 h incubation at 70 °C of HE30 fibrils initially formed at 37 °C. Inset: TEM images of gold nanoparticle superstructures templated by HE30 fibrils show straight assemblies at 37 °C and twisted assemblies at 70 °C.

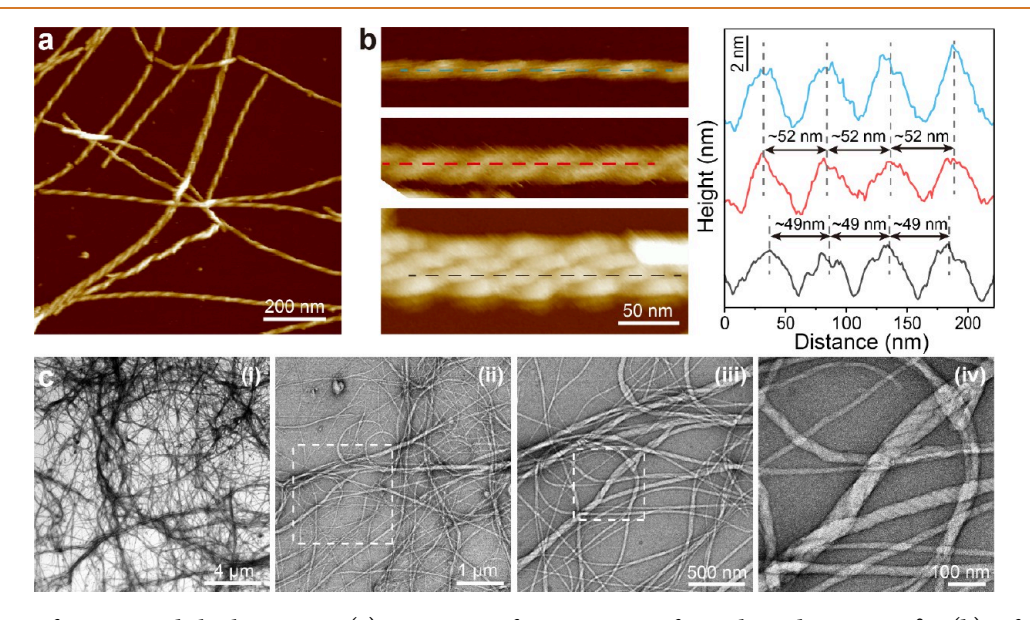


Figure 4. Formation of HE30 superhelical structures. (a) AFM image of $100\,\mu\text{M}$ HE30 after 24 h incubation at $70\,^{\circ}\text{C}$. (b) Left, amplified HE30 structures showing single, double, and four fibril chains; right, height profiles of the section lines indicated in left images. (c) HE30 superhelical structures with zoom-in views highlighting the helical organization.

high stability, remaining intact configuration even after 10 months of storage at room temperature (Figure S10a,b).

Increased Temperature Induces Left-Handed Twisted Transition of HE30 Fibrils. We investigated the effect of temperature on HE30 self-assembly by incubating 100 μ M HE30 at seven temperatures—room temperature (~23 °C), 37, 50, 60, 70, 80, and 90 °C—for 24 h. At room temperature, HE30 formed only a limited number of short fibrils (Figure 3a, Figures S11a and S12a), CD spectroscopy of samples incubated for 24 h at room temperature reveals a significant presence of α -helical structures, indicating a gradual assembly process (Figure 3e and

Figure S11b). Complete assembly into fibrils with lengths up to micrometers required approximately 7 days or more (Figure S11). These fibrils are predominantly straight and nontwisted, with a minor fraction adopting left-handed twisted structures that exhibit a half-pitch length of 67 ± 15 nm (Figure 3a–c, Figure S11).

At 37 °C, HE30 assembled more rapidly, forming a larger quantity of fibrils within 24 h (Figure 3a, Figure S12a). While most fibrils remain nontwisted, the occurrence of twisted structures increased. As the temperature rose, the proportion of twisted fibrils progressively increased, reaching an almost 100%

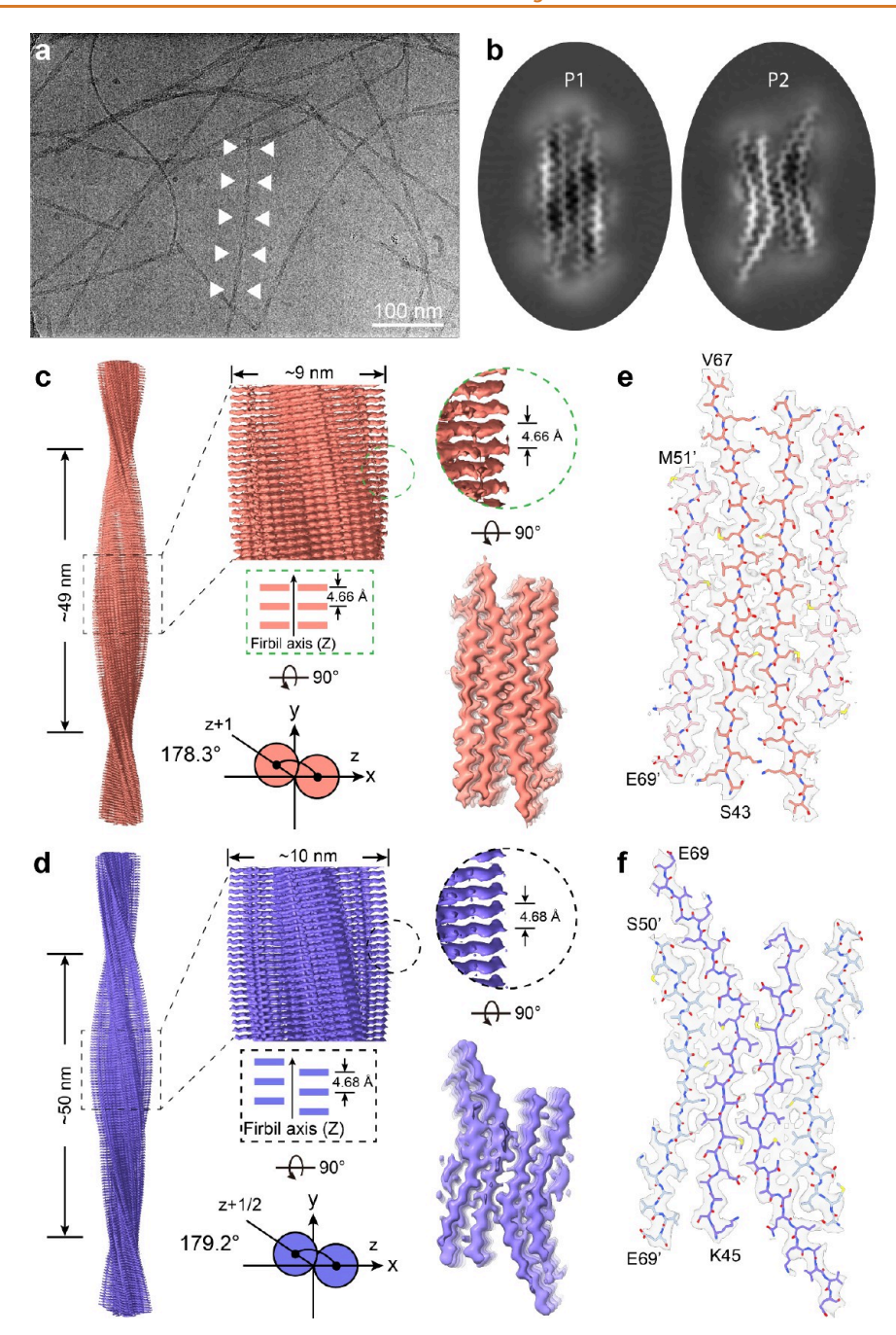


Figure 5. Cryo-EM structures of HE30 twisted fibrils. (a) Cryo-EM micrograph of HE30 twisted fibrils formed at 70 °C with pitch highlighted by white arrows. (b) 3D structural reconstructions of P1 (left) and P2 (right). (c, d) Density maps of P1 (c) and P2 (d) are colored in salmon and blue, respectively. Key fibril parameters including half-pitch, fibril width, twist angle, and helical rise are annotated. (e, f) Structural models of fibrils P1 (e) and P2 (f).

twisted conformation at 70 °C (Figure 3a,c, Figure S12a). Additionally, the twisted pitch shortens with increasing temperature, with a half-pitch of approximately 51 \pm 8 nm observed at 70 °C (Figure 3b). At this temperature, the average fibril length also extends to the micrometer scale, significantly longer than those formed at lower temperatures (Figure 3a,d and Figure S12a). CD spectroscopy indicated that both twisted and nontwisted fibrils feature a β -sheet structure (Figure 3e). The increase in ThT fluorescence intensity with rising temperature further confirmed the β -sheet nature of the formed fibrils (Figure S12b). However, a slight reduction in ThT fluorescence intensity at 70 °C compared to 60 °C likely reflects

fewer available binding sites on the twisted fibrils (Figure S12b). ³⁵ Notably, heating preassembled nontwisted fibrils to 70 °C induced their transformation into twisted fibrils, emphasizing the role of elevated temperature in promoting twisted fibril assembly (Figure 3f). The formed twisted fibrils exhibited high stability, maintaining their structure without disassembly or transitioning back to nontwisted states even after 10 months (Figure S10c). At 80 °C, the quantity of HE30 fibrils diminished markedly; AFM rarely detected fibrils, while negative-stain TEM revealed the formation of a few larger helices composed of multiple twisted fibrils (Figure S13a). Neither AFM nor negative-stain TEM could detect fibril structures when

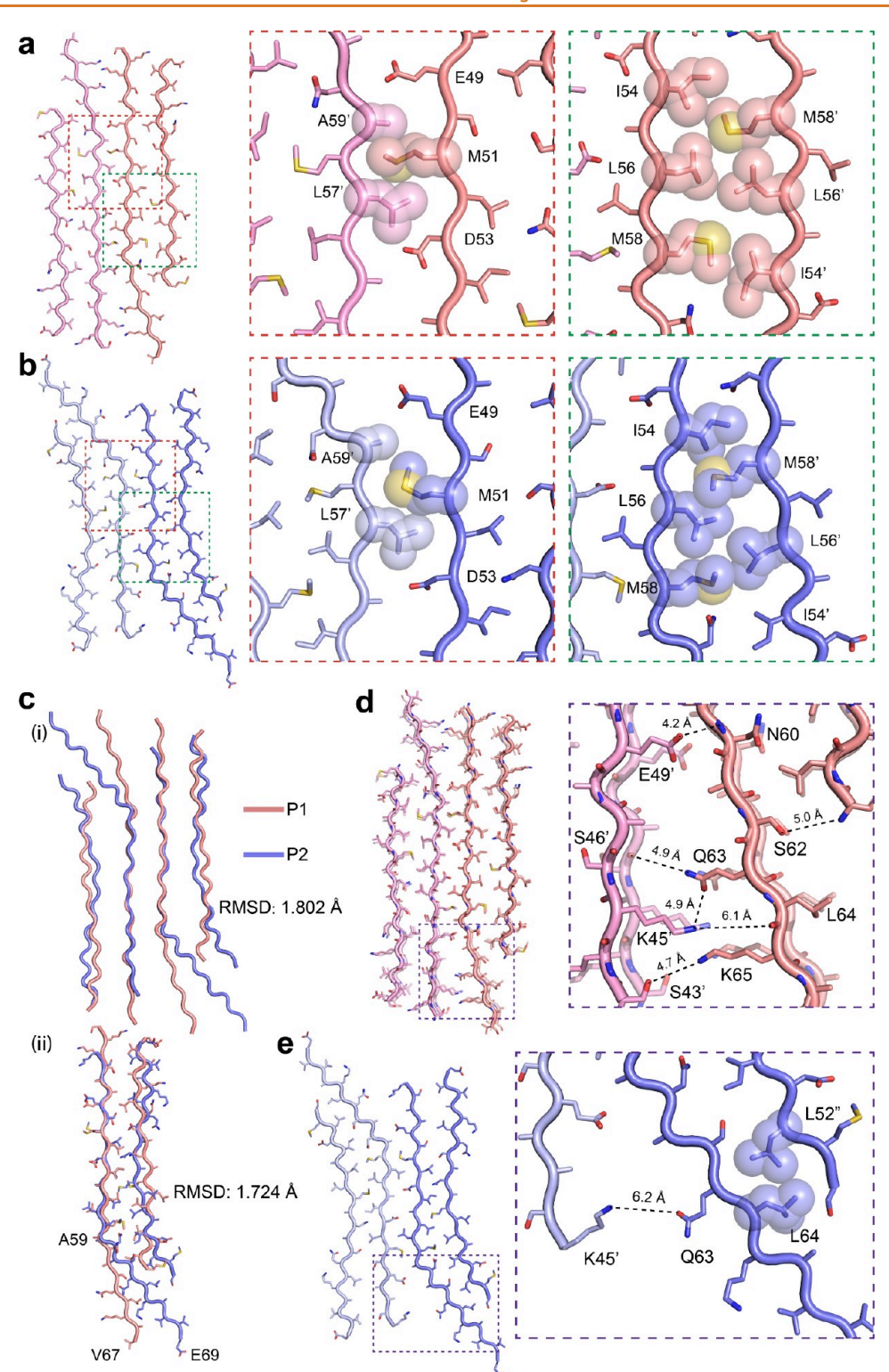


Figure 6. Structural analysis and comparison of HE30 P1 and P2 fibril polymorphs. (a, b) Structural models of P1 (a) and P2 (b) with magnified views highlighting hydrophobic interactions between protofilaments and within individual protofilament. Key residues involved in the interactions are labeled. (c) (i) Comparison of the overall structures of the P1 and P2 protofilament, with RMSD values indicated. (ii) Enlarged view of the structure comparison, emphasizing differences in the C-terminal region (residues A59-E69). (d, e) Detailed views of the electrostatic and hydrophobic interactions at the C-terminal region of P1 (d) and P2 (e), with related residues labeled.

incubated at 90 °C, likely because the peptides were partially denatured at 80 °C and fully denatured at 90 °C (Figure S13b).

To further explore the application of HE30 fibrils, we assessed HE30 fibrils as dynamic templates for colloidal assembly. Owing to their thermoresponsive structural transition, HE30 fibrils

provide a programmable scaffold that directs AuNPs into well-defined superstructures—an approach known to yield geometry-dependent plasmonic coupling, chiroptical activity, hot-spot engineering, and device-relevant transport, with applications in surface-enhanced Raman spectroscopy (SERS) sensing, pho-

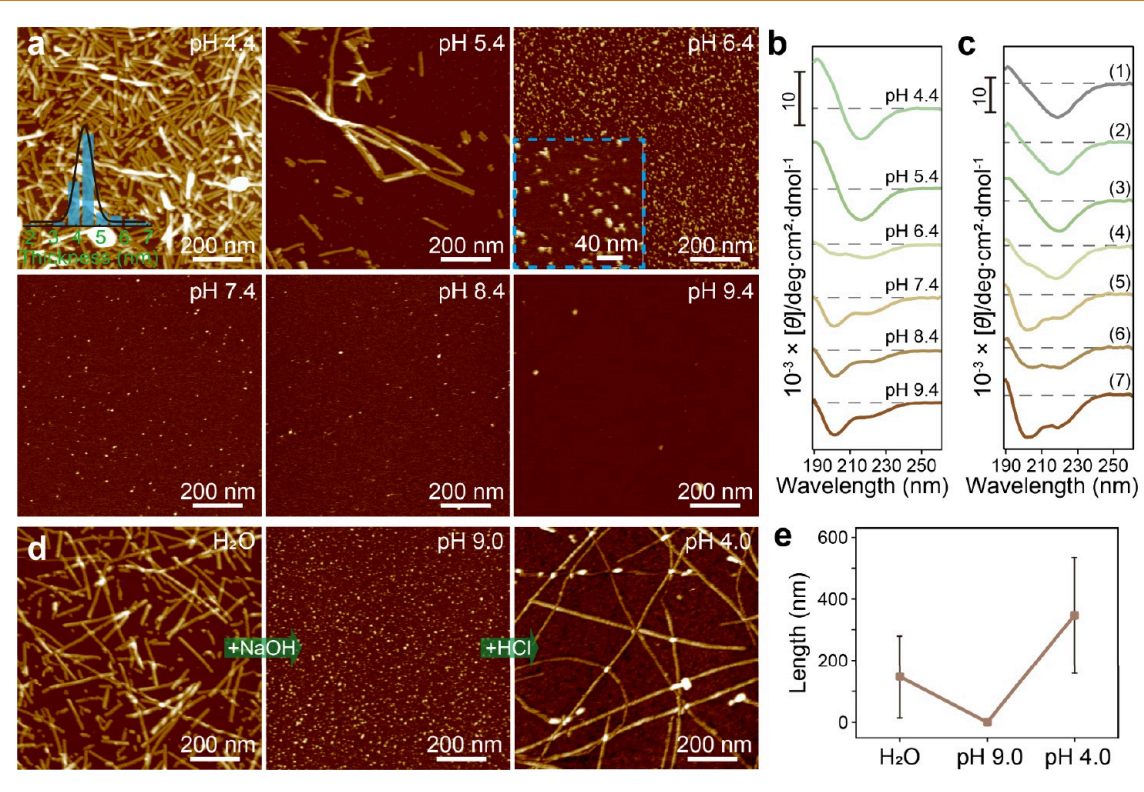


Figure 7. Assembly and disassembly of HE30 fibrils under various pH conditions. (a) AFM images and (b) CD spectra of 100 μ M HE30 after a 24 h incubation at 37 °C across pH buffers of 10 mM sodium acetate (pH 4.4), 10 mM sodium phosphate (pH 5.4), 10 mM Tris-HCl (pH 7.4), 10 mM Tris-HCl (pH 8.4), and 10 mM glycine-sodium hydroxide (pH 9.4). The inset histogram highlights the thickness of HE30 fibrils formed at pH 4.4, while the blue dashed square donates an enlarge view of HE30 assemblies formed at pH 6.4, scale bar: $10^{-2} \times [\theta]/\text{deg·cm²-dmol}^{-1}$. (c) CD spectra of HE30 fibrils preformed in H₂O at 37 °C after a 2 h incubation at room temperature in solutions prepared by 1:1 (v:v) mixing with (1) H₂O, (2) 10 mM sodium acetate (pH 4.4), (3) 10 mM sodium phosphate (pH 5.4), (4) 10 mM sodium phosphate (pH 6.4), (5) 10 mM Tris-HCl (pH 7.4), (6) 10 mM Tris-HCl (pH 8.4), and (7) 10 mM glycine-sodium hydroxide (pH 9.4), scale bar: $10^{-2} \times [\theta]/\text{deg·cm²-dmol}^{-1}$. The results demonstrate that fibrils maintain β -sheet configurations in acidic conditions but transition to an α -helical configuration at neutral or basic pH. (d) AFM images of HE30 fibrils preformed in H₂O at 37 °C (left), after 2 h incubation at pH 9.0 at 70 °C (right), showing reversible structural changes. (e) Statistical analysis of fibril length corresponding to the data in (d), highlighting the reversible nature of fibril assembly and disassembly.

tonics, and nanoscale electronics.^{36–43} At 37 and 70 °C, coincubation of AuNPs with HE30 fibrils led to edge-selective adsorption along the fibril ridges and the emergence of templateguided straight and helical twisted AuNPs superstructures (Figure 3f).

HE30 Hierarchical Self-assembly into Superhelical **Fibril Structures.** The observation of larger helices composed of multiple twisted fibrils at 80 °C inspired us to investigate whether HE30 could form higher-order fibril structures. Given the partial denaturation of HE30 at 80 °C, we extended the incubation time to 45 h at 70 °C. Under this condition, HE30 assembled into superhelical fibrils (Figure 4a,b). Two to four twisted fibrils are intertwined together to form larger helical structures (Figure 4a,b). The half-pitch of fibrils with single and double chains is consistently around 52 nm, but decreases to approximately 49 nm when the chain number increases to four (Figure 4b). With prolonged incubation, these larger helical fibrils underwent further twisting to form hierarchical superhelical fibrils (Figure 4c, Figure S14). These superhelical fibrils can extend up to several tens of micrometers in length and have diameters of several hundred nanometers, with tightly packed, higher-level superhelical fibril structures (Figure 4c, Figure S14).

We further assessed the membrane-disruptive activity and cytotoxicity of HE30 fibrillar assemblies, including nontwisted, twisted, and superhelical forms. Neither membrane disruption,

GUV leakage, nor cytotoxicity toward HEK293T cells was detected (Figures S6b–d, S8b–d, and S15), indicating that HE30 amyloid fibrils either do not interact with membranes or interact only weakly. This stands in contrast to the monomeric state, which exhibits membrane-disruptive activity but only at relatively high concentrations. The spontaneous α -helix–to– β -sheet transition of HE30 monomers into amyloids likely underlies this behavior, as fibril formation diminishes and sequesters the active monomers and thereby diminishing their membrane activity.

Cryo-EM Characterization of HE30 Twisted Fibrils. To further investigate the structural mechanism underlying HE30 fibril self-assembly, we performed cryo-EM to determine the atomic structure of the HE30 fibrils. Due to the technical limitation of cryo-EM helical reconstruction in studying straight, nontwisted fibrils, ^{44–46} we focus on the twisted fibrils formed at 70 °C. This fibril sample was applied to copper grids and rapidly frozen in liquid ethane for cryo-EM data collection. A total of 6,435,335 autopicked particles, derived from 6,243 micrographs, were applied to two-dimensional (2D) classification and subsequent 3D reconstruction (Figure 5a). Intriguingly, 2D classification revealed two major fibril polymorphs, designated as polymorph 1 (P1) and polymorph 2 (P2), comprising approximately 78 and 18% of the sample, respectively (Figure S16a). Both polymorphs displayed a cross-β structure (Figure

5b), rather than an α -helix conformation, with overall resolutions of 2.9 Å for P1 and 3.2 Å for P2 (Figure S16b-d).

P1 and P2 share key structural features, including a left-handed twist, 4 polypeptide chains per layer, antiparallel β -sheet packing across two protofilaments, and an interlayer spacing of ~4.7 Å (Figure 5c,d). However, the two polymorphs differ in their helical symmetries and dimensions. P1 adopts C2 symmetry with a fibril half-pitch of approximately 49 nm (a full pitch corresponding to a 360° helical turn), a fibril width of ~9 nm, and a twist angle of 178.3° between adjacent layers. In contrast, P2 exhibits pseudo-2₁ helical screw symmetry, with a half-pitch of ~50 nm, a fibril width of ~10 nm, and a twist angle of 179.2° between adjacent layers (Figure 5c,d). These fibril half-pitch results obtained from cryo-EM are consistent with AFM measurements (Figure 3a,b).

The spatial arrangements of the polypeptide chains also differ between the two polymorphs. In P1, the chains within the same protofilament are nearly linear, displaying antiparallel packing with differences in chain length (Figure 5e, Figure S17a). In contrast, in P2, the chains are also antiparallel and vary in length but exhibit a slight bending in their conformation (Figure 5f, Figure S17a). The fibril core of P1 comprises residues S43–V67 in the inner long chain and M51–E69 in the outer short chain, while P2 includes residues K45–E69 in the long chain and S50-E69 in the short chain (Figure 5e,f, and Figure S17a,b). Notably, the bending of chains in P2 reduces the interaction interface compared to P1.

Structure Reveals the Self-Assembly of HE30 Fibrils. Further structural analyses were conducted on P1 and P2 fibril polymorphs to identify the molecular interactions governing their fibril structures. Extensive hydrogen bonds between neighboring peptide layers along the fibril axis were observed, playing a crucial role in stabilizing the cross- β structures of both P1 and P2 fibrils (Figure S17c). When comparing peptides from the same layer, despite differences in spatial arrangement, the intermolecular interactions at the protofilament interfaces were found to be similar between P1 and P2 (Figure 6, Figure S17b). Specifically, hydrophobic interactions, formed by residues M51 and L57' & A59' from adjacent chains, stabilize the interface between protofilaments in both P1 and P2 (Figure 6a,b). Additionally, within each protofilament, hydrophobic interactions also play a central role. In P1, six residues (I54, L56, and M58, interacting with M58', L56', and I54' from an adjacent chain) form a zipper-like hydrophobic interaction (Figure 6a). In contrast, P2 involves five residues, including I54, L56, and M58 from one chain and M58' and L56' from an adjacent chain, due to conformational differences (Figure 6b). These hydrophobic interactions are critical to the stability of HE30 fibrils.

Structural comparisons reveal significant conformational similarities between P1 and P2, with root-mean-square deviations (RMSD) of 1.802 Å (over 68 C- α atoms) and 1.724 Å (over 35 C- α atoms), respectively (Figure 6c). The primary difference lies in the C-terminal region (residues A59–E69; Figure 6c). Further analysis of the C-terminal interactions shows that, while both polymorphs are stabilized by electrostatic interactions, the residues involved differ. In P1, multiple electrostatic interactions, including Q63 & K45′, K65 & S43′, and E49′, S62, and Q63 with adjacent backbones, stabilize the interface (Figure 6d). In P2, K45′, Q63, and a hydrophobic interaction between L64 & L52′′ in a distinct region are observed (Figure 6e). Together, cryo-EM structures reveal that the HE30 fibril packing is stabilized by a combination of hydrophobic and electrostatic interactions.

HE30 Fibril Assembly Affected by pH and Salts. Although HE30 fibrils exhibit remarkable stability and are still available even after 10 months at room temperature (Figure S10), the peptide contains pH-sensitive amino acids (H, K, E, and D), and its twisted fibril structures suggest the importance of electrostatic interactions, pointing to potential pH-sensitive assembly properties. To investigate this, we studied HE30 assemblies under various pH conditions. AFM imaging revealed that most fibrils HE30 formed at pH 4.4 are straight and nontwisted after a 24 h incubation at 37 °C (Figure 7a), with a thickness of approximately 4.2 ± 0.6 nm—consistent with fibrils formed in water at 37 °C (Figure 2a,b). CD spectra confirmed that these fibrils retained β -sheet configurations, similar to those formed in water (Figures 7b, 2e, and 3e). These observations indicate that HE30 fibrils formed at pH 4.4 share structural characteristics with those formed in water. The greater abundance of fibrils formed at pH 4.4 compared to water suggests that strongly acidic conditions promote HE30 fibril formation (Figures 7a, 2a, and 3a). As the incubation pH increased, the quantity of fibrils formed decreased (Figure 7a). At pH 6.4, only small, short fibrils were observed. At pH \geq 7.4, HE30 primarily remained as α -helical monomers or formed small oligomers, with minimal fibril formation after a 24 h incubation at 37 °C (Figure 7a,b).

Next, we evaluated the stability of preformed HE30 fibrils under various pH conditions. Fibrils were preformed by incubating 100 μ M HE30 in water at 37 °C for 24 h, followed by 2 h incubation at room temperature in buffers ranging from pH 4.4 to 9.4. CD spectra showed that fibrils retained β -sheet conformations at pH \leq 5.4, but transitioned back to α -helix configurations in neutral or alkaline buffers (Figure 7c). Correspondingly, AFM imaging confirmed that fibrils were stable at pH \leq 5.4 but disassembled at pH \geq 6.4 (Figure S18).

Given these pH-dependent behaviors, we investigated the reversibility of HE30 fibril formation. AFM imaging showed that fibrils preformed in water completely disassembled into nanoparticles after a 2 h incubation at a pH of \sim 9.0 (adjusted with NaOH). However, upon lowering the pH to \sim 4.0 with HCl and incubating for 4.5 days at 37 °C, fibrils reformed (Figure 7d,e). This reversible behavior highlights the importance of hydrogen bonds in the formation and stability of HE30 fibrils. At a pH of \sim 4.0, pH-sensitive amino acids readily form hydrogen bonds, promoting fibril assembly. Conversely, under alkaline conditions, deprotonation disrupts these hydrogen bonds, leading to fibril disassembly.

In addition to pH, buffer salts significantly influence the HE30 fibril assembly. AFM imaging (Figure S19a–d) showed that increasing concentrations of KCl, NaCl, or $CaCl_2$ progressively reduced fibril formation after a 24 h incubation at 37 °C. Statistical analysis of fibril coverage (Figure S19e) confirmed that higher salt concentrations negatively impact HE30 fibril formation, highlighting the role of electrostatic interactions in modulating fibril assembly. Together, these findings indicate acidic conditions (\sim pH 4.4) favor HE30 fibril formation, while neutral or basic conditions and the presence of salts inhibit assembly. These results emphasize the critical role of electrostatic interactions in the assembly and stabilization of HE30 fibrils.

Real-Time Monitoring of HE30 Fibril Growth. We employed *in situ* AFM^{47,48} to monitor the process of HE30 fibril assembly. To overcome the extended incubation time required for HE30 fibril formation at room temperature (Figure S11), we first deposited preformed HE30 fibril seeds onto a

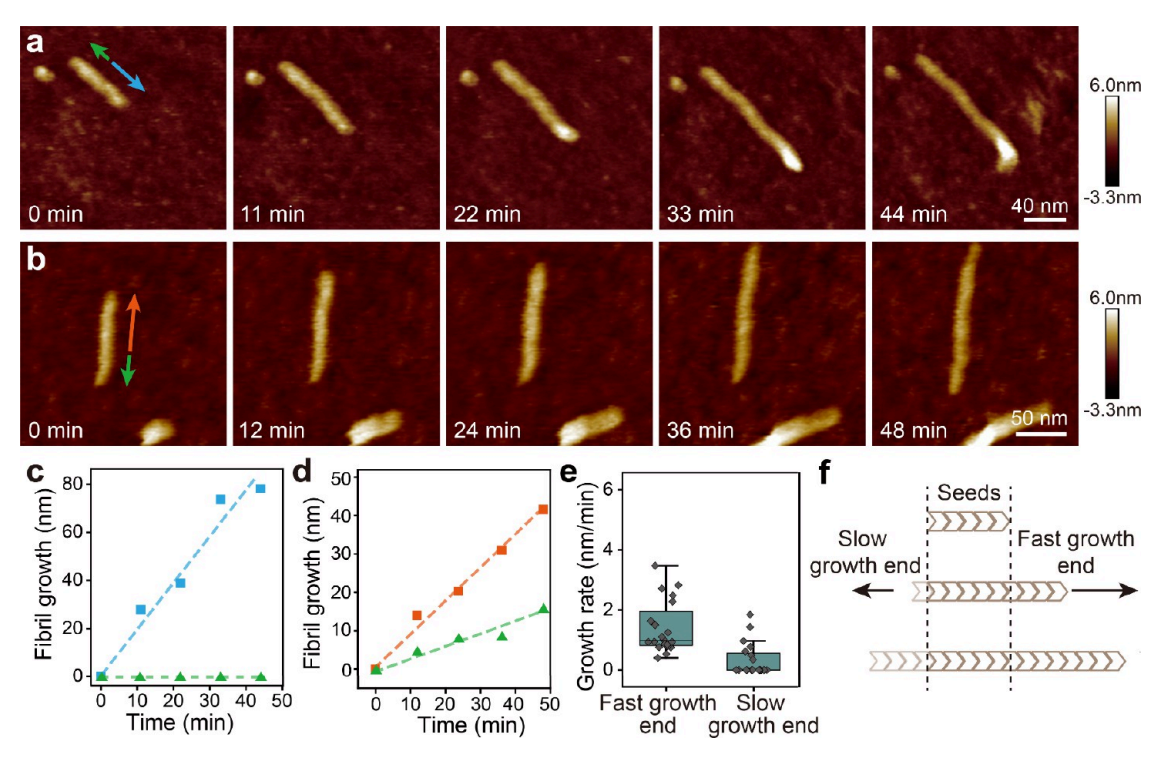


Figure 8. Asymmetric growth of HE30 fibrils. (a, b) Representative AFM images depicting asymmetry fibril growth, where one end exhibits faster elongation (blue arrow in (a), red arrow in (b)) while the other end shows slower growth or inhibition (green arrows). (c, d) Time-course analysis of fibril elongation at the arrow labeled ends in (a) and (b), respectively. The initial fibril length at both ends is defined as 0 at time 0 min. (e) Statistical comparison of the average growth rates for the fast-growing end (total count: 21) and slow-growing end (total count: 21). (f) Proposed molecular mechanism underlying asymmetric seeding reactions at HE30 fibril ends based on the observed differential growth dynamics.

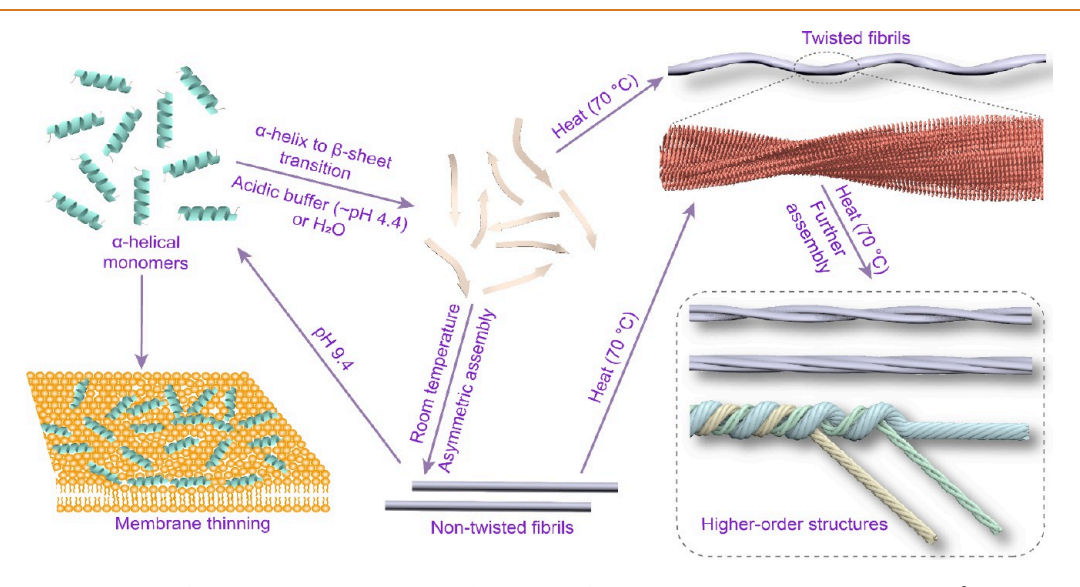


Figure 9. Schematic illustration of the mechanisms underlying the HE30 self-assembly. HE30 undergoes α -helix to β -sheet transitions, leading to hierarchical assembly into nontwisted fibrils, twisted fibrils and subsequently, high-order superhelical structures.

silicon wafer substrate. Subsequently, we added 30 μ M HE30 monomers to initiate fibril elongation and imaged their growth in real time. Notably, asymmetric growth was observed, where one fibril end exhibited faster elongation, while the opposite end displayed slower growth or complete inhibition (Figure 8a, b). The fast-growing end showed an average elongation rate of 1.4 nm/min, which was ~4-fold higher than the slow-growing end (Figure 8c-e). The observed variability in fibril growth rates may be attributed to several factors: (1) Differences in the

efficiency of monomer recruitment by individual fibril seeds, resulting in variable growth rates. ^{49,50} (2) Fibril polymorphism, where structural differences at the two ends may lead to differential monomer binding affinities, with certain configurations potentially hindering monomer attachment. ⁵¹ (3) Intrinsic conformational fluctuations of protein monomers in solution, which can affect their assembly efficiency. ⁵²

DISCUSSION

In this study, we investigated the membrane interaction and selfassembly of HE30, which is the central structural transition domain of NINJ1. We show that HE30 engages lipid membranes in a nonlytic manner. Monomeric HE30 perturbs supported lipid bilayers through bilayer thinning and lipid reorganization (Figures 1 and 9), but induces only minimal dye leakage from GUVs at a peptide-to-lipid ratio of 3:1 and exhibits no cytotoxicity (Figures S6 and S7). This limited activity is likely due to its spontaneous α -helix-to- β -sheet transition in solution, as fibrillar HE30 displays negligible membrane interaction or cytotoxicity (Figures S6, S8, and S15). These findings also reconcile previously reported cargo-release activity, which required unusually high peptide-to-lipid ratios (~157:1).²³ While monomeric HE30 alone does not fully recapitulate the membrane activity of full-length NINJ1, its ability to engage membranes as a single amphipathic chain provides mechanistic insight into the early steps of proteinmembrane interactions during NINJ1-mediated PMR.

A notable discovery is the temperature-dependent morphological transformation of the HE30 fibrils (Figure 9). At physiological temperatures, the fibrils predominantly exhibit a nontwisted structure. However, with increased temperature, these fibrils transition into left-handed twisted forms with tunable pitches and lengths. Moreover, elevated temperatures induce the formation of higher-order superhelical bundles. This dynamic transformation expands our understanding of amyloid aggregation, revealing that fibril morphology can be precisely tuned by temperature. Such tunable behavior holds promise for designing functional amyloid-based materials with customizable mechanical and self-assembly properties.

Helically organized AuNPs represent a key platform in chiral plasmonics, where pitch, particle size, and interparticle distance critically define the strength and spectral position of chiroptical responses. 39-42,39-42,53-55 Hard templates such as silica nanohelices provide robust and uniform scaffolds for site-selective AuNP deposition, while soft templates, including engineered peptides and amyloid fibrils, offer chemical programmability and stimuli-responsiveness that enable dynamic control of chiral assemblies. In this context, we demonstrate that HE30 fibrils function as efficient chiral templates for the organization of AuNPs into both straight and helical superstructures. Unlike conventional scaffolds, HE30 fibrils are biocompatible and fully solution-processable, allowing the AuNP assembly without harsh surface chemistry. Moreover, their intrinsic thermal responsiveness affords reversible switching between straight and helical arrangements. Together, these attributes integrate the stability and programmability of existing platforms with unique stimuli-responsiveness, positioning HE30 fibrils as versatile and biocompatible scaffolds for developing reconfigurable plasmonic and chiroptical nanomaterials.

Cryo-EM analysis identified two distinct polymorphs of HE30 fibrils, differentiated by their helical symmetry and fibril dimensions. Both polymorphs exhibit the characteristic cross- β architecture, with one polymorph (P1) adopting C2 symmetry and the other (P2) displaying pseudo- 2_1 helical screw symmetry. The ability of HE30 to form multiple polymorphs under identical environmental conditions highlights the inherent structural plasticity of amyloid fibrils. This polymorphism likely influences fibril stability, aggregation dynamics, and potential interactions with cellular components or biomolecules, under-

scoring the biological and functional significance of amyloid heterogeneity.

HE30 fibrils exhibit high stability, remaining intact without disassembly even after 10 months at room temperature. However, environmental factors, particularly pH and ionic strength, play crucial roles in regulating the self-assembly of HE30 fibrils. Acidic conditions (\sim pH 4.4) favor fibril formation, driven by enhanced hydrophobic interactions and electrostatic interactions, while alkaline conditions lead to rapid disassembly into α -helical monomers due to disruption of these interactions, especially hydrogen bonds. The inhibitory effect of salts further underscores the critical role of electrostatic interactions in fibril stabilization. These findings suggest that modulating pH and ionic strength offers a viable strategy for controlling fibril assembly and disassembly, paving the way for developing functional amyloid nanomaterials such as drug delivery systems.

Real-time AFM imaging revealed asymmetric fibril growth with one end elongating faster than the other. This directional growth suggests that fibril formation is a dynamic and nonuniform process, driven by differential monomer recruitment at fibril ends. Understanding this asymmetric growth mechanism provides valuable insights into amyloid assembly and offers a potential framework for designing amyloid-based nanostructures with predictable geometries and functionalities.

Our structural and functional dissection of HE30 integrates diverse aspects of amyloid biology while advancing several fronts. In the amyloid field, phenomena such as helix-to- β transitions, fibrillar polymorphism, electrostatic regulation by pH and ionic strength, and asymmetric growth kinetics have been observed in both pathological and functional systems. However, these principles are rarely comprehensively characterized within a single protein or peptide, leaving many fundamental mechanisms of amyloid formation and toxicity incompletely understood. Here, HE30—the N-terminal fragment of NINJ1—bridges these properties by coupling an α helical, monomeric, nonlytic membrane-remodeling state to a reversibly assembled cross- β state, whose polymorphs we resolve by cryo-EM. Temperature modulates twist and hierarchical supercoiling, while acidity promotes, and salts or bases suppress, assembly, highlighting a dominant electrostatic grammar layered atop hydrophobic interactions. Subtle adjustments of temperature, pH, and incubation time enable precise control over the helical pitch, diameter, and handedness of the resulting chiral nanostructures. Real-time AFM reveals strongly polarized elongation, consonant with asymmetric end kinetics seen for $A\beta$, but in a peptide whose native role is related to membrane rupture. This decoupling of monomers from inert fibrils, together with the ability to template AuNP superstructures, establishes HE30 as a minimal, stimuli-programmable amyloid platform that extends current models of polymorphism and function.

CONCLUSIONS

In conclusion, this study delineates the membrane interactions and distinctive self-assembly properties of HE30, a NINJ1-derived peptide capable of reversible α -helix—to— β -sheet transitions and polymorphic fibril formation. In its monomeric state, HE30 engages lipid bilayers in a nonlytic manner, reorganizing membranes and modulating properties such as thickness. In aqueous solution, HE30 spontaneously assembles into nontwisted, twisted, and bundled fibrils, which undergo temperature-dependent transformations into two additional polymorphs with C2 symmetry and pseudo-21 helical screw

symmetry. The fibrils further exhibit asymmetric growth dynamics with differential elongation rates at opposing ends. Temperature-dependent nontwist—to—twist transitions, together with reversible pH-driven assembly and disassembly, position HE30 as a minimal platform for engineering environmentally responsive amyloid materials. Moreover, coincubation with AuNPs at 37 and 70 °C yields template-guided straight and helically twisted AuNP superstructures through edge-selective adsorption along fibril ridges.

MATERIALS AND METHODS

Sample Preparation. One mg portion of synthesized HE30 (98.69%, GL Biochem, Shanghai, China) was dissolved in 100 μ L of 1% acetonitrile (ACN). A 2 μ L aliquot of this solution was then mixed with 63.5 μ L of distilled water and 0.5 μ L of ACN to prepare 66 μ L of 100 μ M HE30 solution containing 0.8% ACN. For temperature-dependent experiments, peptide solutions were incubated at temperatures ranging from 23 to 90 °C for 24 h or the indicated times. For the helical transition experiment, preformed HE30 fibrils (66 µL 100 µM HE30 was incubated at 37 °C for 14 days) were incubated at 70 °C for 1 day. For pH-dependent assembly experiments, distilled water was replaced with buffer solutions and incubated at 37 °C for 1 day or the indicated times. The pH values of buffer solutions used were as follows: pH 4.4 (10 mM Sodium acetate), pH 5.4 (10 mM Sodium phosphate), pH 6.4 (10 mM Sodium phosphate), pH 7.4 (10 mM Tris-HCl), pH 8.4 (10 mM Tris-HCl), and pH 9.4 (10 mM Glycine-Sodium hydroxide). For acid-base stability experiments, preformed HE30 fibrils (66 µL 100 μM HE30 incubated in water at 37 °C for 14 days) were mixed with equal volumes of buffers ranging from pH 4.4 to 9.4, followed by 2 h $\,$ incubation at room temperature. For the reversibility assembly of HE30 fibril, fibrils were preformed by incubating 66 μ L of 100 μ M HE30 in water at 37 °C for 24 h were adjusted with 50 mM NaOH to a pH of ~9.0, followed by a 2 h incubation at room temperature. The pH was subsequently adjusted to pH ~4.0 using 500 mM HCl and then incubated for 4.5 days at 37 °C. For salt-dependent experiments, HE30 was dissolved in 0.8% ACN solutions containing 1 mM, 10 mM, 100 mM, or 1 M KCl, NaCl, or CaCl₂. The samples were then incubated at 37 °C for 24 h before testing. For in situ experiments, HE30 fibril seeds were initially preformed by incubating 10 μ M HE30 in 0.8% ACN for 24 h at room temperature. Subsequently, 5 μ L of the preformed fibrils were deposited onto a clean silicon wafer substrate $(4 \times 4 \text{ mm in size})$. Fresh 10 μ L of 30 μ M HE30 monomers were added to the substrate to track fibril growth in real time at room temperature. Preparation of AuNP superstructures: HE30 fibrils were prepared by incubating a 100 μM HE30 solution at 37 or 70 °C for 24 h. To assemble AuNP superstructures, 7 μ L of the fibril suspension was mixed with 3 μ L of 0.1 mg mL⁻¹ citrate-capped gold nanoparticles. The mixture was incubated in the dark for 3 h and subsequently stored at room temperature.

HPLC and MS. The peptide samples were analyzed by HPLC on a Gemini-NX C18 column (5 μ m, 4.6 × 250 mm). The mobile phase consisted of 0.1% trifluoroacetic acid (TFA) in acetonitrile (ACN) and 0.1% TFA in water. The total flow rate was maintained at 1.0 mL min⁻¹, with a UV detection at 220 nm. MS analysis was performed on a Shimadzu LCMS-2020 instrument using ESI mode.

SEC. The molecular weight distribution of HE30 was analyzed using a Waters HPLC system equipped with a BioCore SEC-120 column (5 μ m, 7.8 × 300 mm, NanoChrom). HE30 (1 mg) was dissolved in 3 mL of 0.8% acetonitrile (ACN), and 5 μ L of the solution was injected. The mobile phase consisted of 150 mM phosphate buffer (pH 6.8) at a flow rate of 0.7 mL/min. The column temperature was maintained at 25 °C, and the UV absorbance was monitored at 214 nm. Molecular weight calibration was performed by using standard proteins and peptides: BSA (66,430 Da), IgG (150,000 Da), cytochrome c (12,365 Da), Ala-Tyr-Glu-Val-Asp (595 Da), and tyrosine (181 Da).

Preparation of SLBs. The method for SLB formation was detailed in our previous studies and followed a standardized procedure. ^{56–59} In brief, the lipids obtained from Avanti Polar Lipids were dissolved in chloroform, mixed with DOPC:DOPS:DOPE = 8:1:1. All the lipid

compositions used in this work are shown in mass ratios. The mixture was then dried using argon flow in a small glass vial, followed by >2 h incubation in a vacuum desiccator. Subsequently, lipids were fully rehydrated with buffer (20 mM HEPES-NaOH, pH 7.4, 150 mM NaCl) for 5 min at room temperature, with the volume adjusted to achieve a lipid solution at 0.5 mg/mL. Next, the lipid suspension was either bath-sonicated for 45 min or tip sonicated for ~4 min to obtain a clear small unilamellar vesicle (SUV) solution. Finally, 1 μ L 5 mM CaCl₂ and 5 μ L of lipid solution were deposited onto a freshly cleaved 2.2 mm diameter mica disk, incubated for over 30 min to form largely covered SLBs, and rinsed thoroughly with buffer (20 mM HEPES-NaOH, pH 7.4, 150 mM NaCl).

High-Speed Atomic Force Microscopy (HS-AFM). HS-AFM imaging was performed at room temperature by adding 313 μ M (1 mg/mL) HE30 monomers to preformed lipid SLBs (DOPC:DOPS:DOPE = 8:1:1, wt), which were then directly imaged by HS-AFM. All images in this study were acquired using an HS-AFM (SS-NEX, RIBM, Japan) operated in amplitude modulation mode. Eight μ m short cantilevers (USC-F1.2-k0.15, NanoWorld, Switzerland) with a nominal spring constant of 0.15 N/m, a resonance frequency of ~0.6 MHz, and a quality factor of ~1.5 in imaging buffer (20 mM HEPES-NaOH, pH 7.4, 150 mM NaCl) were used. HS-AFM movies were processed using ImageJ 1.52, and plane fitting was applied to flatten the images.

Atomic Force Microscopy (AFM). A 5 μ L drop of the HE30 sample was applied to freshly cleaved mica (1.5 mm in diameter) for 10 min. The mica surface was then washed five times with distilled water and imaged in distilled water. For HE30–SLB interaction experiments, 20 μ L of 100 μ M HE30 monomer or fibrils was added to SLBs, and real-time changes were monitored by AFM imaging. AFM imaging was conducted using tapping mode with Bruker SNL-10 A/B/C/D triangular probes (nominal spring constant: k = 0.35, 0.12, 0.24, 0.08 N/m) at room temperature on a Bruker Multimode 8 AFM system

Negative-Stain Transmission Electron Microscopy (TEM). A 5 μ L portion of the HE30 sample was dropped onto a glow-discharged copper grid coated with parlodion and carbon and left for 5 min at room temperature. The grid was then washed with 300 μ L of distilled water, followed by staining with 7.5 μ L 1% uranyl acetate for 2 min and blotting dry with filter paper. Negative-stained images were collected by using either a JEOL2100 microscope operating at 200 kV or a JEOL JEM-1011 microscope operating at 100 kV.

Cryo-EM Sample Preparation and Data Collection. A 635 μ L solution of 100 μ M HE30 in 0.8% ACN was incubated at 70 °C for 24 h and then concentrated to approximately 60 μ L. A 3 μ L aliquot of the concentrated sample was deposited onto Quantifoil R1.2/1.3 300 Au holey carbon grids (Quantifoil), and the grid was then blotted and frozen in liquid ethane using a Vitrobot Mark IV (FEI). The grids were stored in liquid nitrogen for further use. Data collection was performed on a 300 kV Titan Krios (FEI) microscope equipped with a K3 summit detector (Gatan) and a Gatan imaging filter (GIF) with a slit of 20 eV. Automatic data acquisition was carried out using SerialEM software. The data were collected in super-resolution mode with a physical pixel size of 1.04 Å. The dose rate was set to 13.7 e⁻/pixel/s, and the total exposure time was 4.8 s. Each micrograph was divided into 40 frames. A total of 7180 micrographs were collected for the HE30 peptide.

Image Processing. The MotionCorr2⁶¹ for motion correction was performed to correct beam-induced motion of movie frames with doseweighting. Next, CTFFIND-4.1.8⁶² was used to estimate the contrast transfer function of motion-corrected images. Only micrographs with resolution beyond 5 Å, which were estimated by CTFFIND-4.1.8, were applied to the following 3D reconstruction in RELION version 3.1.⁶³

Helical Reconstruction. A small part of fibrils was manually picked by using the manual picking method of RELION 3.1,⁶³ and its two-dimensional (2D) classification results were used for autopicking. The autopicking results were applied to the helical reconstruction in RELION 3.1,⁶³ including particle extraction, 2D classification, 3D classification, 3D autorefinement, CTF refinement, Bayesian polishing, and postprocessing.

After autopicking and particle extraction, 6,435,335 particles from 6243 selected high-quality micrographs in 288 pixels box-size were applied to several iterations of 2D classification at the T=2

regularization parameter to purify particles. Then, a cylindrical map model generated by the RELION helix toolbox program was used as an initial 3D reference to perform the following 3D classification (K = 3) for both 2 classes. When the local search of symmetry for helical twist and rise was carried out after the separation of β -strands, the clearest class was selected for the following data processing. 3D classification, 3D autorefinements, Bayesian polishing, and CTF refinement were repeated for two rounds to obtain better helical reconstruction results. Finally, the overall resolutions of two classes of fibrils were reported at 2.9 and 3.2 Å, based on the gold-standard FSC = 0.143 criteria.

Atomic Model Building and Refinement. Using the density maps after the postprocessing program, the atomic models of two classes of fibril were built de novo in COOT,⁶⁴ respectively. Then, three-layer models were generated in software Chimera or ChimeraX and refined by a real-space refinement program in PHENIX.^{65,66} Additional details about the two models are shown in Table S3.

Circular Dichroism. For Figure 1h, 100 μ L of 100 μ M HE30 in water with 0.8% ACN was prepared after incubation at 37 °C for 0, 3, 6, 9, 12, 15, 18, 21, or 24 h. For Figure S2, 122 μ L of 50 μ M D-HE30 was dissolved in 0.8% ACN and measured immediately. For Figure 2e, 200 μL of 250 μM HE30 was prepared after 24 h of incubation at temperatures of 23, 37, 50, 60, or 70 °C. For Figure S4, 100 μ L of 100 μ M HE30 was prepared after incubation at room temperature for 0, 1, 3, 7, 10, or 13 days. For Figure 6b, 200 μ L of 100 μ M HE30 was prepared after 24 h of incubation at 37 °C in buffers (containing 0.8% ACN) with pH values of 4.4, 5.4, 6.4, 7.4, 8.4, or 9.4. The pH buffer solutions used were as follows: pH 4.4 (10 mM sodium acetate), pH 5.4 (10 mM sodium phosphate), pH 6.4 (10 mM sodium phosphate), pH 7.4 (10 mM Tris-HCl), pH 8.4 (10 mM Tris-HCl), and pH 9.4 (10 mM glycine-sodium hydroxide). For Figure 6c, HE30 fibrils, preformed by incubation of 100 μ L of 100 μ M HE30 at 37 °C for 24 ĥ, were mixed with equal volumes of buffers ranging from pH 4.4 to 9.4, followed by 2 h of incubation at room temperature. The CD spectrum was measured with a Chirascan plus spectrometer (Applied Photophysics, U.K.) from 190 to 260 nm with a 1 mm optical path.

Thioflavin T (THT) Fluorescence Measurements. For Figure 1g, 500 μ L of 100 μ M HE30 monomers or preformed fibrils (prepared by incubating 500 μ L of 100 μ M HE30 in water (containing 0.8% ACN) at 37 °C for 24 h) was mixed with 500 μ L of 400 μ M ThT, resulting in a final 1 mL of 50 μ M HE30 and 200 μ M ThT. The mixtures were coincubated at room temperature for 2 h prior to measurement. For Figure S5b, 500 μ L of 100 μ M HE30 monomers were incubated at 23, 37, 50, 60, or 70 °C for 24 h and then mixed with 500 μ L of 400 μ M ThT to achieve a final concentration of 50 μ M HE30 and 200 μ M ThT in a 1 mL solution. These samples were also coincubated for 2 h at room temperature before measurement. The ThT fluorescence spectra were recorded using an FS5 spectrofluorometer (Edinburgh Instruments, UK) with an excitation wavelength of 450 nm.

GUVs Leakage. GUVs with a composition of DOPC: DOPS: DOPE: Liss rhod PE (18:1) = 8:1:1:0.005 (Avanti Polar Lipids, Inc.) were produced via electroformation using the Vesicle Prep Pro (Nanion Technologies). 67 10 μ L 2 mg/mL lipid mixtures in chloroform were deposited within an 18 mm O-ring chamber mounted on an indium tin oxide (ITO) electrode and placed in a vacuum chamber for 2 h. Subsequently, the O-ring chamber was filled with about 200 μ L of 200 mM sucrose solution (shielded from light with aluminum foil), and the Vesicle Prep Pro machine was operated using a standardized protocol (37 °C, 100 Hz, 7.5 V, 10 min Rise, 120 min Main, 30 min Fall). The resultant GUVs were stored in a small glass bottle at 4 °C.

Before the addition of HE30, 90 μ L of mixed liquid (containing 80 μ L of GUVs with a composition of DOPC:DOPS:DOPE:Liss rhod PE (18:1) = 8:1:1:0.005 in sucrose, 10 μ L of 10 μ M FITC-dextran (Sigma-Aldrich)) was dispensed on the glass-bottom dish. Ten μ L of 3.13 mM HE30 monomers, HE30 nontwisted fibrils formed at 37 °C, HE30 twisted fibrils formed at 70 °C, and HE30 superhelical fibrils formed at 70 °C for 2 days were then introduced to the mixed solution. The GUVs were imaged with a confocal fluorescence microscope (FV3000, Olympus) and processed with Fiji (ImageJ).

Cell Viability Assay. A549 (CL-0016), MRC-5 (CL-0161), NCI-H1299 (CL-0165), NCI-H460 (CL-0299), and HEK293T cell lines were obtained from Procell Life Science & Technology (Wuhan, China). A549 cells were cultured in Ham's F-12K medium supplemented with 10% fetal bovine serum (FBS) and 1% penicillin–streptomycin. MRC-5 cells were maintained in Modified Eagle's Medium (MEM) with 10% FBS and 1% penicillin–streptomycin. NCI-H1299 and NCI-H460 cells were grown in RPMI 1640 medium (Gibco, USA) supplemented with 10% FBS and 1% penicillin–streptomycin. HEK293T cells were cultured in 88% high-glucose DMEM, 10% FBS, and 2% penicillin dihydrate. All cells were maintained at 37 °C in a humidified incubator with 5% CO₂.

Cell proliferation was assessed using CCK-8 (Beyotime, China) according to the manufacturer's instructions. Briefly, 1×10^4 cells were seeded into each well of a 96-well flat-bottomed plate and incubated for 24 h. Cells were then treated with HE30 monomers or fibrils at the indicated concentrations for an additional 24 h. Subsequently, 10 $\mu \rm L$ of CCK-8 solution was added to each well and incubated for 2 h at 37 °C. Absorbance at 450 nm was measured using a microplate reader (Thermo Fisher Scientific). Each experiment was performed independently in triplicate.

ASSOCIATED CONTENT

Supporting Information

The Supporting Information is available free of charge at https://pubs.acs.org/doi/10.1021/acsnano.5c14731.

HPLC and MS analysis of HE30; structure predication and alignment of HE30 domain; SEC and AFM characterization of HE30 monomers; CD characterization of D-HE30 monomers; confocal fluorescence microscopy tracking of GUV leakage induced by HE30; cytotoxicity assay of HE30; TEM image of HE30 coincubated with ThT; AFM characterization of the stability of HE30 fibrils; AFM and CD spectra of HE30 fibrils after incubation of 0, 1, 3, 7, 10, 13 days at room temperature; TEM images and ThT fluorescence of HE30 assembly after 24 h incubation at temperatures of 23, 37, 50, 60, or 70 °C; AFM and TEM images of HE30 after 24 h incubation at 80 and 90 °C; AFM images of HE30 after 45 h incubation at 70 °C; in situ AFM images showing that HE30 fibrils do not disrupt supported lipid bilayers; cryo-EM structures of HE30 helical fibrils; structure models and sequence analysis of HE30 fibrils in comparison with NINJ1; AFM characterization of acidbase stability of HE30 fibrils; AFM characterization of the effects of different salts on HE30 fibril assembly; cryo-EM data collection, modeling, and refinement statistics (PDF)

HE30 induced bilayer thinning of only a few angstroms without detectable pore formation (AVI)

AUTHOR INFORMATION

Corresponding Authors

Jian-Ping Zhang — Key Laboratory of Advanced Light
Conversion Materials and Biophotonics, School of Chemistry
and Life Resources, Renmin University of China, Beijing
100872, China; ⊙ orcid.org/0000-0002-9216-2386;
Email: jpzhang@ruc.edu.cn

Cong Liu — Interdisciplinary Research Center on Biology and Chemistry, Shanghai Institute of Organic Chemistry, Chinese Academy of Sciences, Shanghai 201210, China; State Key Laboratory of Chemical Biology, Shanghai Institute of Organic Chemistry, Chinese Academy of Sciences, Shanghai 200032, China; ⊚ orcid.org/0000-0003-3425-6672; Email: liulab@sioc.ac.cn

Fang Jiao — Beijing National Laboratory for Condensed Matter Physics, Institute of Physics, Chinese Academy of Sciences, Beijing 100190, China; ⊚ orcid.org/0000-0001-5087-6228; Email: fang.jiao@iphy.ac.cn

Authors

- Meijiao Wang Beijing National Laboratory for Condensed Matter Physics, Institute of Physics, Chinese Academy of Sciences, Beijing 100190, China; Key Laboratory of Advanced Light Conversion Materials and Biophotonics, School of Chemistry and Life Resources, Renmin University of China, Beijing 100872, China
- Wencheng Xia Interdisciplinary Research Center on Biology and Chemistry, Shanghai Institute of Organic Chemistry, Chinese Academy of Sciences, Shanghai 201210, China; University of Chinese Academy of Sciences, Beijing 100049, China; ⊚ orcid.org/0000-0002-2100-7055
- Dan Zhao Beijing National Laboratory for Condensed Matter Physics, Institute of Physics, Chinese Academy of Sciences, Beijing 100190, China; Department of Pharmacy, JiangXi University of Traditional Chinese Medicine, JiangXi 330004, China
- Zhaoyi Zhai Beijing National Laboratory for Condensed Matter Physics, Institute of Physics, Chinese Academy of Sciences, Beijing 100190, China; State Key Laboratory of Medicinal Chemical Biology, College of Pharmacy, Nankai University, Tianjin 300350, China
- Rongjing Chen Beijing National Laboratory for Condensed Matter Physics, Institute of Physics, Chinese Academy of Sciences, Beijing 100190, China; University of Chinese Academy of Sciences, Beijing 100049, China
- Xue Bai State Key Laboratory of Membrane Biology, School of Life Sciences, Peking University, Beijing 100871, China
- Zhe Zhang State Key Laboratory of Membrane Biology, School of Life Sciences and Center for Life Sciences, Academy for Advanced Interdisciplinary Studies, Peking University, Beijing 100871, China
- Hao Fan Department of Pharmacy, JiangXi University of Traditional Chinese Medicine, JiangXi 330004, China

Complete contact information is available at: https://pubs.acs.org/10.1021/acsnano.5c14731

Author Contributions

[†]These authors contributed equally: M.-J.W. and W.X.

Author Contributions

F.J., C.L., and J.Z. designed and conceptualized the study. M.W. and F.J. performed the AFM experiments and analyzed the data. F.J. and R.C. performed the TEM experiments. D.Z. and M.W. performed the CD experiments. X.B. and M.W. performed the Cryo-EM experiments. W.X. built and refined models of HE30 fibrils. H.F. and Z.Z. analyzed and interpreted the results. F.J. wrote the manuscript with input from all authors.

Notes

The authors declare no competing financial interest.

ACKNOWLEDGMENTS

The authors sincerely appreciate Dr. Wei Ding for the fruitful discussion and detailed suggestions on this work. The authors thank Professor Meining Zhang, Dr. Shuai Zhang, and Ms. Xinyue Wang for their assistance with cell viability assay experiments. This research was funded by the National Natural Science Foundation of China (NSFC 92353304, T2221001,

32371525, and T2350011 to F.J.; 82188101, 22425704, and 32171236 to C.L.), the Strategic Priority Research Program of the Chinese Academy of Sciences (XDB37020105 to F.J.; XDB1060000 to C.L.), the Science and Technology Commission of Shanghai Municipality (STCSM) (grant no. 22JC1410400 to C.L.), Shanghai Basic Research Pioneer Project to C.L., the Shanghai Pilot Program for Basic Research — Chinese Academy of Science, Shanghai Branch (grant no. JCYJSHFY-2022-005 to C.L.), and the CAS Project for Young Scientists in Basic Research (grant no.YSBR-095 to C.L.).

REFERENCES

- (1) Malik, S.; Yadav, J. K. Amyloids and Amyloid-like Protein Aggregates in Foods: Challenges and New Perspectives. *Curr. Protein Pept. Sci.* **2023**, *24*, 393–403.
- (2) Levkovich, S. A.; Gazit, E.; Laor Bar-Yosef, D. Two Decades of Studying Functional Amyloids in Microorganisms. *Trends Microbiol.* **2021**, 29, 251–265.
- (3) Blanco, L. P.; Evans, M. L.; Smith, D. R.; Badtke, M. P.; Chapman, M. R. Diversity, Biogenesis and Function of Microbial Mmyloids. *Trends Microbiol.* **2012**, *20*, 66–73.
- (4) Sergeeva, A. V.; Galkin, A. P. Functional Amyloids of Eukaryotes: Criteria, Classification, and Biological Significance. *Curr. Genet.* **2020**, 66, 849–866.
- (5) Wang, X. Y.; Zhang, S. N.; Zhang, J. C.; Wang, Y. M.; Jiang, X. Y.; Tao, Y. Q.; Li, D.; Zhong, C.; Liu, C. Rational Design of Functional Amyloid Fibrillar Assemblies. *Chem. Soc. Rev.* **2023**, *52*, 4603–4631.
- (6) Hardy, J.; Selkoe, D. J. The Amyloid Hypothesis of Alzheimer's Disease: Progress and Problems on the Road to Therapeutics. *Science* **2002**, 297, 353–6.
- (7) Singleton, A. B.; Farrer, M.; Johnson, J.; Singleton, A.; Hague, S.; Kachergus, J.; Hulihan, M.; Peuralinna, T.; Dutra, A.; Nussbaum, R.; Lincoln, S.; Crawley, A.; Hanson, M.; Maraganore, D.; Adler, C.; Cookson, M. R.; Muenter, M.; Baptista, M.; Miller, D.; Blancato, J.; et al. Alpha-Synuclein Locus Triplication Causes Parkinson's Disease. *Science* 2003, 302, 841.
- (8) Anguiano, M.; Nowak, R. J.; Lansbury, P. T., Jr. Protofibrillar Islet Amyloid Polypeptide Permeabilizes Synthetic Vesicles by a Pore-like Mechanism that May Be Relevant to Type II Diabetes. *Biochemistry* **2002**, *41*, 11338–43.
- (9) Knowles, T. P.; Vendruscolo, M.; Dobson, C. M. The Amyloid State and Its Association with Protein Misfolding Diseases. *Nat. Rev. Mol. Cell. Biol.* **2014**, *15*, 384–96.
- (10) Fowler, D. M.; Koulov, A. V.; Balch, W. E.; Kelly, J. W. Functional Amyloid-from Bacteria to Humans. *Trends Biochem. Sci.* **2007**, *32*, 217–224.
- (11) Barnhart, M. M.; Chapman, M. R. Curli Biogenesis and Function. *Annu. Rev. Microbiol.* **2006**, *60*, 131–147.
- (12) Arnaouteli, S.; Bamford, N. C.; Stanley-Wall, N. R.; Kovacs, A. T. Biofilm Formation and Social Interactions. *Nat. Rev. Microbiol.* **2021**, 19, 600–614.
- (13) Rouse, S. L.; Matthews, S. J.; Dueholm, M. S. Ecology and Biogenesis of Functional Amyloids in Pseudomonas. *J. Mol. Biol.* **2018**, 430, 3685–3695.
- (14) Liu, X. P.; Liang, C.; Zhang, X. K.; Li, J. Y.; Huang, J. Y.; Zeng, L.; Ye, Z. H.; Hu, B. R.; Wu, W. J. Amyloid Fibril Aggregation: An Insight into The Underwater Adhesion of Barnacle Cement. *Biochem. Bioph. Res. Commun.* **2017**, 493, 654–659.
- (15) Franzmann, T. M.; Jahnel, M.; Pozniakovsky, A.; Mahamid, J.; Holehouse, A. S.; Nuske, E.; Richter, D.; Baumeister, W.; Grill, S. W.; Pappu, R. V.; Hyman, A. A.; Alberti, S. Phase Separation of a Yeast Prion Protein Promotes Cellular Fitness. *Science* **2018**, 359, No. eaao5654.
- (16) Maji, S. K.; Perrin, M. H.; Sawaya, M. R.; Jessberger, S.; Vadodaria, K.; Rissman, R. A.; Singru, P. S.; Nilsson, K. P. R.; Simon, R.; Schubert, D.; Eisenberg, D.; Rivier, J.; Sawchenko, P.; Vale, W.; Riek, R. Functional Amyloids As Natural Storage of Peptide Hormones in Pituitary Secretory Granules. *Science* **2009**, 325, 328–332.

- (17) Li, J. X.; McQuade, T.; Siemer, A. B.; Napetschnig, J.; Moriwaki, K.; Hsiao, Y. S.; Damko, E.; Moquin, D.; Walz, T.; McDermott, A.; Chan, F. K. M.; Wu, H. The RIP1/RIP3 Necrosome Forms a Functional Amyloid Signaling Complex Required for Programmed Necrosis. *Cell* **2012**, *150*, 339–350.
- (18) Hoppenreijs, L. J. G.; Fitzner, L.; Ruhmlieb, T.; Heyn, T. R.; Schild, K.; van der Goot, A. J.; Boom, R. M.; Steffen-Heins, A.; Schwarz, K.; Keppler, J. K. Engineering Amyloid and Amyloid-like Morphologies of β -lactoglobulin. *Food Hydrocolloids* **2022**, *124*, No. 107301.
- (19) Brändén, C.-I.; Tooze, J. Introduction to Protein Structure. 2nd ed.; Garland Pub.: New York, 1999; pp 410.
- (20) Araki, T.; Zimonjic, D. B.; Popescu, N. C.; Milbrandt, J. Mechanism of Homophilic Binding Mediated by Ninjurin, a Novel Widely Expressed Adhesion Molecule. *J. Biol. Chem.* **1997**, 272, 21373–21380.
- (21) Araki, T.; Milbrandt, J. Ninjurin, a Novel Adhesion Molecule, Is Induced by Nerve Injury and Promotes Axonal Growth. *Neuron* **1996**, *17*, 353–361.
- (22) Liu, K.; Wang, Y.; Li, H. The Role of Ninjurin1 and Its Impact beyond the Nervous System. *Dev. Neurosci.* **2021**, 42, 159–169.
- (23) Kayagaki, N.; Kornfeld, O. S.; Lee, B. L.; Stowe, I. B.; O'Rourke, K.; Li, Q.; Sandoval, W.; Yan, D.; Kang, J.; Xu, M.; Zhang, J.; Lee, W. P.; McKenzie, B. S.; Ulas, G.; Payandeh, J.; Roose-Girma, M.; Modrusan, Z.; Reja, R.; Sagolla, M.; Webster, J. D.; et al. NINJ1Mediates Plasma Membrane Rupture During lytic Cell Death. *Nature* **2021**, *591*, 131–136.
- (24) Ramos, S.; Hartenian, E.; Santos, J. C.; Walch, P.; Broz, P. NINJ1 Induces Plasma Membrane Rupture and Release of Damage-associated Molecular Pattern Molecules During Ferroptosis. *EMBO J.* **2024**, 43, 1164–1186.
- (25) Han, J. H.; Karki, R.; Malireddi, R. K. S.; Mall, R.; Sarkar, R.; Sharma, B. R.; Klein, J.; Berns, H.; Pisharath, H.; Pruett-Miller, S. M.; Bae, S. J.; Kanneganti, T. D. NINJ1Mediates Inflammatory Cell Death, PANoptosis, and Lethality during Infection Conditions and Heat Stress. *Nat. Commun.* **2024**, *15*, 1739.
- (26) Ramos, S.; Hartenian, E.; Broz, P. Programmed Cell Death: NINJ1 and Mechanisms of Plasma Membrane Rupture. *Trends Biochem. Sci.* **2024**, *49*, 717–728.
- (27) Kayagaki, N.; Stowe, I. B.; Alegre, K.; Deshpande, I.; Wu, S.; Lin, Z.; Kornfeld, O. S.; Lee, B. L.; Zhang, J.; Liu, J.; Suto, E.; Lee, W. P.; Schneider, K.; Lin, W.; Seshasayee, D.; Bhangale, T.; Chalouni, C.; Johnson, M. C.; Joshi, P.; Mossemann, J.; et al. Inhibiting Membrane Rupture with NINJ1 Antibodies Limits Tissue Injury. *Nature* 2023, 618, 1072–1077.
- (28) Pourmal, S.; Truong, M. E.; Johnson, M. C.; Yang, Y.; Zhou, L.; Alegre, K.; Stowe, I. B.; Gupta, S.; Chen, P. A.; Zhang, Y.; Rohou, A.; Newton, K.; Kayagaki, N.; Dixit, V. M.; Deshpande, I. Autoinhibition of Dimeric NINJ1 Prevents Plasma Membrane Rupture. *Nature* **2025**, 637, 446–452.
- (29) Degen, M.; Santos, J. C.; Pluhackova, K.; Cebrero, G.; Ramos, S.; Jankevicius, G.; Hartenian, E.; Guillerm, U.; Mari, S. A.; Kohl, B.; Mueller, D. J.; Schanda, P.; Maier, T.; Perez, C.; Sieben, C.; Broz, P.; Hiller, S. Structural Basis of NINJ1-mediated Plasma Membrane Rupture in Cell Death. *Nature* 2023, 618, 1065–1071.
- (30) David, L.; Borges, J. P.; Hollingsworth, L. R.; Volchuk, A.; Jansen, I.; Garlick, E.; Steinberg, B. E.; Wu, H. NINJ1Mediates Plasma Membrane Rupture by Cutting and Releasing Membrane Disks. *Cell* **2024**, *187*, 2224–2235.
- (31) Sahoo, B.; Mou, Z.; Liu, W.; Dubyak, G.; Dai, X. How NINJ1Mediates Plasma Membrane Rupture and Why NINJ2 Cannot. *Cell* **2025**, *188*, 292–302.
- (32) Melo, M. N.; Ferre, R.; Castanho, M. A. R. B. Antimicrobial Peptides: Linking Partition, Activity and High Membrane-bound Concentrations. *Nat. Rev. Microbiol.* **2009**, *7*, 245–250.
- (33) Portelinha, J.; Duay, S. S.; Yu, S. I.; Heilemann, K.; Libardo, M. D. J.; Juliano, S. A.; Klassen, J. L.; Angeles-Boza, A. M. Antimicrobial Peptides and Copper(II) Ions: Novel Therapeutic Opportunities. *Chem. Rev.* **2021**, *121*, 2648–2712.

- (34) Hammond, K.; Ryadnov, M. G.; Hoogenboom, B. W. Atomic Force Microscopy to Elucidate How Peptides Disrupt Membranes. *Biochim. Biophys. Acta, Biomembr.* **2021**, *1863*, No. 183447.
- (35) Wu, C.; Biancalana, M.; Koide, S.; Shea, J. E. Binding Modes of Thioflavin-T to the Single-layer Beta-sheet of the Peptide Self-assembly Mimics. *J. Mol. Biol.* **2009**, *394*, *627*–33.
- (36) Schulz, F.; Pavelka, O.; Lehmkühler, F.; Westermeier, F.; Okamura, Y.; Mueller, N. S.; Reich, S.; Lange, H. Structural Order in Plasmonic Superlattices. *Nat. Commun.* **2020**, *11*, 3821.
- (37) Bian, K. F.; Schunk, H.; Ye, D. M.; Hwang, A.; Luk, T. S.; Li, R. P.; Wang, Z. W.; Fan, H. Y. Formation of Self-assembled Gold Nanoparticle Supercrystals with Facet-dependent Surface Plasmonic Coupling. *Nat. Commun.* **2018**, *9*, 2365.
- (38) Kim, J.; Zhao, Q.; Choi, I.; Oh, M. J.; Kwon, S.; Park, S. Ensemble Hot-spots in 3D Supercrystals of Plasmonic Octahedral Nanoparticles in Tip-to-tip Configured Superlattices. *Nat. Commun.* **2025**, *16*, 2762.
- (39) Merg, A. D.; Boatz, J. C.; Mandal, A.; Zhao, G. P.; Mokashi-Punekar, S.; Liu, C.; Wang, X. T.; Zhang, P. J.; van der Wel, P. C. A.; Rosi, N. L. Peptide-Directed Assembly of Single-Helical Gold Nanoparticle Superstructures Exhibiting Intense Chiroptical Activity. *J. Am. Chem. Soc.* **2016**, *138*, 13655–13663.
- (40) Vila-Liarte, D.; Kotov, N. A.; Liz-Marzán, L. M. Template-assisted Self-assembly of Achiral Plasmonic Nanoparticles into Chiral Structures. *Chem. Sci.* **2022**, *13*, 595–610.
- (41) Matricardi, C.; Hanske, C.; Garcia-Pomar, J. L.; Langer, J.; Mihi, A.; Liz-Marzán, L. M. Gold Nanoparticle Plasmonic Superlattices as Surface-Enhanced Raman Spectroscopy Substrates. *ACS Nano* **2018**, 12, 8531–8539.
- (42) Cheng, J. J.; Le Saux, G.; Gao, J.; Buffeteau, T.; Battie, Y.; Barois, P.; Ponsinet, V.; Delville, M. H.; Ersen, O.; Pouget, E.; Oda, R. GoldHelix: Gold Nanoparticles Forming 3D Helical Superstructures with Controlled Morphology and Strong Chiroptical Property. *ACS Nano* 2017, 11, 3806–3818.
- (43) Chen, C. L.; Rosi, N. L. Preparation of Unique 1-D Nanoparticle Superstructures and Tailoring their Structural Features. *J. Am. Chem. Soc.* **2010**, *132*, 6902–6903.
- (44) Li, D.; Liu, C. Structural Diversity of Amyloid Fibrils and Advances in Their Structure Determination. *Biochemistry* **2020**, *59*, 639–646.
- (45) Shi, Y.; Zhang, W.; Yang, Y.; Murzin, A. G.; Falcon, B.; Kotecha, A.; van Beers, M.; Tarutani, A.; Kametani, F.; Garringer, H. J.; Vidal, R.; Hallinan, G. I.; Lashley, T.; Saito, Y.; Murayama, S.; Yoshida, M.; Tanaka, H.; Kakita, A.; Ikeuchi, T.; Robinson, A. C.; et al. Structure-based Classification of Tauopathies. *Nature* **2021**, *598*, 359–363.
- (46) Yang, Y.; Shi, Y.; Schweighauser, M.; Zhang, X.; Kotecha, A.; Murzin, A. G.; Garringer, H. J.; Cullinane, P. W.; Saito, Y.; Foroud, T.; Warner, T. T.; Hasegawa, K.; Vidal, R.; Murayama, S.; Revesz, T.; Ghetti, B.; Hasegawa, M.; Lashley, T.; Scheres, S. H. W.; Goedert, M. Structures of α -synuclein Filaments from Human Brains with Lewy Pathology. *Nature* **2022**, *610*, 791–795.
- (47) Jiao, F.; Wu, X.; Jian, T.; Zhang, S.; Jin, H.; He, P.; Chen, C. L.; De Yoreo, J. J. Hierarchical Assembly of Peptoid-Based Cylindrical Micelles Exhibiting Efficient Resonance Energy Transfer in Aqueous Solution. *Angew. Chem., Int. Ed. Engl.* **2019**, 58, 12223–12230.
- (48) Zhai, Z.; Schmid, S. Y.; Lin, Z.; Zhang, S.; Jiao, F. Unveiling the Nanoscale Architectures and Dynamics of Protein Assembly with in situ Atomic Force Microscopy. *Aggregate* **2024**, *5*, No. e604.
- (49) Eisenberg, D.; Jucker, M. The Amyloid State of Proteins in Human Diseases. *Cell* **2012**, *148*, 1188–1203.
- (50) Pinotsi, D.; Buell, A. K.; Galvagnion, C.; Dobson, C. M.; Kaminski Schierle, G. S.; Kaminski, C. F. Direct Observation of Heterogeneous Amyloid Fibril Growth Kinetics via Two-Color Super-Resolution Microscopy. *Nano Lett.* **2014**, *14*, 339–345.
- (51) Meinhardt, J.; Sachse, C.; Hortschansky, P.; Grigorieff, N.; Fändrich, M. $A\beta(1-40)$ Fibril Polymorphism Implies Diverse Interaction Patterns in Amyloid Fibrils. *J. Mol. Biol.* **2009**, 386, 869–877.
- (52) Watanabe-Nakayama, T.; Nawa, M.; Konno, H.; Kodera, N.; Ando, T.; Teplow, D. B.; Ono, K. Self- and Cross-Seeding on α -

- Synuclein Fibril Growth Kinetics and Structure Observed by High-Speed Atomic Force Microscopy. ACS Nano 2020, 14, 9979–9989.
- (53) Gansel, J. K.; Thiel, M.; Rill, M. S.; Decker, M.; Bade, K.; Saile, V.; von Freymann, G.; Linden, S.; Wegener, M. Gold Helix Photonic Metamaterial as Broadband Circular Polarizer. *Science* **2009**, 325, 1513–1515.
- (54) Song, C. Y.; Blaber, M. G.; Zhao, G. P.; Zhang, P. J.; Fry, H. C.; Schatz, G. C.; Rosi, N. L. Tailorable Plasmonic Circular Dichroism Properties of Helical Nanoparticle Superstructures. *Nano Lett.* **2013**, 13, 3256–3261.
- (55) Kuzyk, A.; Schreiber, R.; Fan, Z. Y.; Pardatscher, G.; Roller, E. M.; Högele, A.; Simmel, F. C.; Govorov, A. O.; Liedl, T. DNA-based Self-assembly of Chiral Plasmonic Nanostructures with Tailored Optical Response. *Nature* **2012**, *483*, 311–314.
- (56) Jiao, F.; Ruan, Y.; Scheuring, S. High-speed Atomic Force Microscopy to Study Pore-forming Proteins. *Methods Enzymol.* **2021**, 649, 189–217.
- (57) Ni, T.; Jiao, F.; Yu, X. L.; Aden, S.; Ginger, L.; Williams, S. I.; Bai, F. F.; Prazak, V.; Karia, D.; Stansfeld, P.; Zhang, P. J.; Munson, G.; Anderluh, G.; Scheuring, S.; Gilbert, R. J. C. Structure and Mechanism of Bactericidal Mammalian Perforin-2, an Ancient Agent of Innate Immunity. *Sci. Adv.* **2020**, *6*, No. eaax8286.
- (58) Jiao, F.; Dehez, F.; Ni, T.; Yu, X. L.; Dittman, J. S.; Gilbert, R.; Chipot, C.; Scheuring, S. Perforin-2 clockwise Hand-over-hand Prepore to Pore Transition Mechanism. *Nat. Commun.* **2022**, *13*, 5039.
- (59) Ren, K.; Farrell, J. D.; Li, Y.; Guo, X.; Xie, R.; Liu, X.; Kang, Q.; Fan, Q.; Ye, F.; Ding, J.; Jiao, F. Mechanisms of RCD-1 Pore Formation and Membrane Bending. *Nat. Commun.* **2025**, *16*, 1011.
- (60) Mastronarde, D. N. Automated Electron Microscope Tomography Using Robust Prediction of Specimen Movements. *J. Struct. Biol.* **2005**, *152*, 36–51.
- (61) Zheng, S. Q.; Palovcak, E.; Armache, J. P.; Verba, K. A.; Cheng, Y.; Agard, D. A. MotionCor2: Anisotropic Correction of Beam-induced Motion for Improved Cryo-electron Microscopy. *Nat. Methods* **2017**, *14*, 331–332.
- (62) Rohou, A.; Grigorieff, N. CTFFIND4: Fast and Accurate Defocus Estimation from Electron Micrographs. *J. Struct. Biol.* **2015**, 192, 216–221.
- (63) Zivanov, J.; Nakane, T.; Forsberg, B. O.; Kimanius, D.; Hagen, W. J.; Lindahl, E.; Scheres, S. H. New Tools for Automated Highresolution Cryo-EM Structure Determination in RELION-3. *eLife* **2018**, *7*, No. e42166.
- (64) Emsley, P.; Lohkamp, B.; Scott, W. G.; Cowtan, K. Features and Development of Coot. *Acta Crystallogr. Sect. D Struct. Biol.* **2010**, *66*, 486–501
- (65) Adams, P. D.; Afonine, P. V.; Bunkoczi, G.; Chen, V. B.; Davis, I. W.; Echols, N.; Headd, J. J.; Hung, L. W.; Kapral, G. J.; Grosse-Kunstleve, R. W.; McCoy, A. J.; Moriarty, N. W.; Oeffner, R.; Read, R. J.; Richardson, D. C.; Richardson, J. S.; Terwilliger, T. C.; Zwart, P. H. PHENIX: a Comprehensive Python-based System for Macromolecular Structure Solution. *Acta Crystallogr. Sect. D Struct. Biol.* **2010**, *66*, 213—21.
- (66) Afonine, P. V.; Poon, B. K.; Read, R. J.; Sobolev, O. V.; Terwilliger, T. C.; Urzhumtsev, A.; Adams, P. D. Real-space Refinement in PHENIX for Cryo-EM and Crystallography. *Acta Crystallogr. Sect. D Struct. Biol.* **2018**, *74*, 531–544.
- (67) Ma, L.; Hu, S. X.; He, X. L.; Yang, N.; Chen, L. C.; Yang, C. G.; Ye, F. F.; Wei, T. T.; Li, M. Detection of tBid Oligomerization and Membrane Permeabilization by Graphene-Based Single-Molecule Surface-Induced Fluorescence Attenuation. *Nano Lett.* **2019**, *19*, 6937–6944.

